Computational Analysis of Tensile Damage and Failure of Mineralized Tissue Assisted with Experimental Observations

Anil Misra[1,2,3*], Rizacan Sarikaya[2,3]

[1]Civil, Environmental and Architectural Engineering Department, [2]Mechanical Engineering Department, [3]Institute for Bioengineering Research
University of Kansas, 1530 W. 15th Street, Learned Hall, Lawrence, KS 66045-7609.
*corresponding author: Ph: (785) 864-1750, Fax: (785) 864-5631, Email: amisra@ku.edu

Proceedings of the Institution of Mechanical Engineers, Part H: Journal of Engineering in Medicine

Abstract

In this study, deformation and failure mechanisms of mineralized tissue (bone) were investigated both experimentally and computationally by performing diametral compression tests on millimetric disc specimens and conducting finite element (FE) analysis where a granular micromechanics based nonlinear user defined material model is implemented. The force-displacement relationship obtained in the simulation agreed well with the experimental results. The simulation was also able to capture location of the failure initiation observed in the experiment which is inside out from the hole along the loading axis. Furthermore, propagation of micro-sized cracks into failure was observed both in the experiment using simultaneous slow-motion microscopy imaging and in the simulation analyzing the local distortion and local volume change within the specimen. The anisotropy evolution was found to be significant around the hole along the loading axis by evaluating the anisotropy index computed using FE results. In conclusion, this work revealed that the prediction capability of granular micromechanics based user defined nonlinear material model is promising considering the match between the results and observations from the physical experiment and FE analysis such as force-displacement relationship and failure initiation/pattern. This work has also shown that the tensile damage and failure of mineralized tissues can be characterized using diametral compression (split tension) test.

Keywords: damage; failure; mineralized tissue; indirect tensile test; bone mechanics; finite element modeling; granular micromechanics.

Introduction

The damage evolution and failure of mineralized tissues is a key aspect of its mechanical behavior. Characterization of fracture/damage behavior of mineralized tissue (such as dentin and bone) under tensile loading is fraught with challenges. These challenges include issues such as scale dependency (due to hierarchical structure spanning the spatial scales), sample preparation and uncertainties associated to the boundary conditions. In the case of human dentin particularly, the sample preparation is rather sensitive due to the smallness and spatial variability of the original tissue. Therefore, on one hand the traditional uniaxial tensile tests can be difficult to perform, and on the other hand, bending tests and indentation tests can be difficult to interpret, especially to explicate the behavior under tension. The conventional tensile strength test results depend upon various factors such as specimen geometry, its size and application of load or boundary conditions [1]. Applying pure tensile load on stick specimen to achieve uniform distributions of loads in their cross-section can be challenging. In some cases the specimen are glued to the loading blocks. The factors involved in adhesion procedure contribute to uncertainties associated with boundary conditions. Enduring adhesion requires consideration of surface roughness and cleanliness, wetting and contact angle, providing sufficient flow of adhesive and issues related to phase separation and solidification of adhesive [2]. Due to the nature of brittle materials, direct tensile tests also suffers from stress concentrations where the sample is gripped by or attached to the loading device [3]. These stress concentrations can result in premature failure of specimen in the grips [4]. The consequence is that there are many uncertainties associated with devising continuum constitutive laws for modeling the damage and failure of these materials.

In this context it is interesting to observe that recent careful experiments have shown that failure in these materials is preceded by development of dilatation band at nano-scales which

manifests as the so-called diffuse damage at the scale of mineralized collagen fibril that appear to form micro-sized cracks that then coalesce into a failure zone (fracture) [5]. Such observations are reminiscent of behavior shown by cementitious and other granular materials, whose behavior is characterized by loading path-dependent damage evolution and localization into dilation or shear zone [6, 7]. Given that at their building-block scales these tissues have a distinct granular nature comprised of interacting nano-sized mineral crystallite mediated by nano-sized collagen fibers (although many other structural details intervene between these scales and the scale at which continuum properties are specified), there are strong imperatives to treat them from a granular micromechanics viewpoint.

Granular micromechanics approach provides a paradigm for modeling materials in which the microstructure and micromechanical properties play significant role in defining the macroscopic behavior of the material. In this approach, the material representative volume element (RVE) is envisioned as a collection of grains which are interacting with each other through different inter-granular mechanisms. As noted in afore cited work on formation of nano-dilatational bands [5], the fracture necessarily involves collective behavior of many grains and is not represented by separation or shear failure of a grain-pair. The macroscopic behavior of the material in granular micromechanics is derived as an average response of the variously oriented grain-pair interactions. The result is that local or micro-level mechanism are captured in the continuum constitutive laws albeit in an average sense. In this work two issues are addressed: (1) characterization of tensile damage and failure of these tissues using split tension test on millimetric samples, and (2) verification of granular micromechanics based continuum constitutive law for modeling split tension test of mineralized tissue.

Materials and Methods

For the experimental characterization, cortical bone tissue derived from a bovine femur was used as an example of mineralized tissue. Bovine cortical bone tissue provides the compositional similarities with many dense mineralized tissue, such as dentin, [8], although its hierarchical structure may have certain uniqueness. Tensile damage evolution and failure were measured using diametral compression test. These tests have also been performed recently on tissue specimen derived from teeth and have been found to give significantly different and less variable tensile strength compared to conventional tests [9] [10] [11]. To interpret the results from our diametral compression test, we have used numerical simulation of the test by employing the constitutive model based upon granular micromechanics [7] as a UMAT in commercial finite element analysis software (Simulia/ABAQUS V 6.13-3, Dassault Systémes, RI, USA).

Sample Preparation

Cortical bone tissue was derived from a bovine femur which was freshly procured from a local slaughterhouse. The femur was coarsely dissected using a hand saw and the cortical bone tissue was extracted from the sections within the diaphysis of the bone using a diamond saw cutting machine (Isomet 1000, Buehler, Lake Bluff, IL). Test specimens were machined using a drill press (Drill Press 4212, WEN, Elgin, IL) attached with a core drill bit initially into a cylindrical shape and then a hole was drilled in the center attaching a drill bit to the drill press using a laser for alignment. Lastly, the cylinder was cut into discs using the diamond saw cutting machine and then stored in phosphate-buffered saline solution with pH of 7.4 (Sigma-Aldrich, St. Louis, MO) and ~0.1 wt% sodium azide, and refrigerated for a week. Such storage is known to mimic in vivo conditions and prevent surface demineralization by preserving the specimen in the physiological range of pH where the composition of the solution is close to tissue fluid [12]. Additionally, the

specimen was preferred to be kept refrigerated in the solution since the frozen water within the specimen would lead to unnatural brittle behavior if the specimen was kept frozen. The samples were hydrated through all machining processes. All disc specimens have the diameter of 3 mm and the thickness of 0.6 mm, with a central hole of diameter 1 mm.

Diametral Compression Test

The indirect tensile test or Brazilian test overcomes several drawbacks of conventional tensile test. The indirect tensile test was separately invented by Carneiro and Barcellos in Brazil and by Akazawa in Japan [13-15]. It is also called as diametral compression test or the split tensile test [16]. The Brazilian test has been applied widely to measure tensile strength of rock [17], concrete [18], cohesive soils [16], pressed metal powder [19], pharmaceutical tablets [20], human enamel [10] and also bonding strength of concentric composites in dental research [9]. The procedure of indirect tensile test is relatively simple both in sample preparation and load application on the sample since it does not require to fix the sample to any grips and the sample is conveniently loaded by placing it between two parallel load blocks.

The test is conducted by compressing the disc sample along its diameter between the two parallel load blocks [16] as shown in Fig. 1. In Fig. 1a, a schematic diagram is presented for the diametral compression test. Fig. 1b gives an image of the microtensile test stage with the sample placed upon the load platens. The test on millimetric disc specimen were performed using Microtest stage (Microtest 200N Stage, Deben UK Ltd., Bury St Edmunds, UK) with jaws specifically fabricated for diametral compression test (Fig. 1b). The test was conducted by ensuring that the load platens are aligned parallel to each other. The inset in Fig. 1b gives a close-up image showing the placement of the specimen and the parallel alignment of the load platens. The loading was applied as displacement with the rate of 0.2 mm/min and load-displacement data were recorded via data

acquisition system. The specimen was video imaged during the load application via in-house built slow-motion video recording microscopy setup (240 frames per second, 1280x720 pixels). These images will be analyzed in the future using digital image correlation or other image analysis techniques for obtaining field measurements.

The diametral compression loading results in the development of tensile action perpendicular to the loading axis [19]. In a departure from the classical diametral compression test, we utilize disc sample with a central hole as illustrated in Fig. 1a. The hole provides prescribed weakness location to promote diametral failure in randomly heterogeneous defective materials such as bones. For future improvement in sample preparation, a lathe may be used to precisely place a hole in the center of specimen since the current method results in a small offset in the hole position (amplified by the parallax in the picture due to camera angle). In our experience, the experimental result was not significantly affected by the small offset in the hole position.

Numerical Analysis

Numerical analysis was carried out implementing the granular micromechanics based user defined nonlinear material model into the commercial finite element analysis software (Simulia/ABAQUS V 6.13-3, Dassault Systémes, RI, USA). The required geometry, boundary conditions, loading and material property parameters were selected according to the experimental application (Fig. 1a).

Material Model

The user defined nonlinear material model is created based on granular micromechanics approach to establish constitutive equations for cementitious materials [7]. We consider this as suitable approach owing to the granular nature of bone, in which the nano-sized apatitic mineral grains interact with each other with the mediation of the collagen molecules. Additionally, the

granular micromechanics better captures the anisotropy evolution and volume change behavior in granular materials [7] in contrast to the numerous elasto-plastic laws proposed in the literature. In the granular micromechanics model, macroscopic dissipation potential and Helmholtz free energy density functions are expressed using the volume averages of matching functions from grain-pair interactions. The model uses a Clausius-Duhem type inequality in order to represent proper constitutive relationships for grain-pair. Furthermore, constitutive equations in micro scale are calibrated in order the macro-scale material behavior corresponds to the experimental behavior. It was shown that for material's with granular texture, the behavior at the macro scale strongly depends on loading path resulting from nonlinear intergranular force laws and that each intergranular contact undergo unique loading history in different directions [7, 21].

Following the work described in[7, 22] the listed material model parameters (Table 1) are selected for bovine cortical bone where E^{T}_{n0} is grain scale normal stiffness in tension, R is ratio of compression to tension in terms of grain scale elastic stiffness, G_w is grain scale elastic stiffness in shear. The physical meaning of the model parameters are depicted in Fig. 2 [7].

User-defined nonlinear material model parameters	Bovine cortical bone
E^{T}_{no}	7 N/mm
R	12
G_w	2 N/mm
B_n	$7\text{x}10^{-4}$ mm
B_{wo}	$1.32\text{x}10^{-3}$ mm

α_1	10.5
α_2	7
α_3	0.0012
α_4	0.0265 MPa^{-1}

Table 1 Material parameters for bovine cortical bone.

B_n is inter-granular displacement where normal inter-granular force reaches to peak in tensile inter-granular force-displacement curve, B_{w0} is inter-granular shear yield parameter in tension, α_1, α_2 and α_3 are model parameters of creating shear damage parameter with respect to normal displacement in micro scale and α_4 is stiffness growth parameter related to the increase in confinement. We note that the parameters in Table 1, have been refined for bovine bone starting from those based upon previous work with concrete [7], accounting for the limited data available in the literature for bovine femur[32] where the authors have performed traditional compression and tension test (using 5 mm long specimen for compression and dumb-bell style 35 mm long specimen for tension). We further note that the data in the literature for complete stress-strain behavior of cortical bovine bone is characteristically rare, particularly under 3D or complex loading conditions. There is data of tension-compression yield and ultimate strength of human cortical bone under uniaxial tests[33] as well as for enamel[10] specimen tested under diametral compression (using disk of 2.5mm diameter and 1.25 mm thick). The refined parameters are qualitatively compatible with these data as well in terms of the tension-compression asymmetry, strain to failure/yield and peak stresses under uniaxial tension and compression. The revised and recalibrated parameters are able to simulate the behavior of bovine cortical bone, although it is interesting that some of the parameters remained same as that for concrete.

This model has the earlier foundation starting with[21]. Thermomechanical formulation is established for rate-dependent material with damage and plasticity where Clausius-Duhem inequality is derived as the following:

$$p^i - \dot{W} - S\dot{\theta} - \frac{q_k \theta_{,k}}{\theta} = d \geq 0 \tag{1}$$

Where W is Helmholtz free energy, S is entropy per unit volume, θ is the thermodynamic temperature, q_k is the heat flux vector and d is the dissipation per unit volume. p^i is the power density function which is $p^i = \sigma_{ij}\dot{\varepsilon}_{ij}$, derived using the Cauchy stress and the symmetric part of first gradient of displacement.

For the rate dependent material with damage and plasticity, the Helmholtz free energy density is expressed as the following function: $W = W(\varepsilon_{ij}, \varepsilon_{ij}^v, D_{ij}, \varepsilon_{ij}^p, \theta)$ where ε_{ij} is the independent kinematic variable, ε_{ij}^v is the rate-dependent phenomenon related internal variable, D_{ij} is the damage related internal variable and ε_{ij}^p is the plasticity related internal variable [21]. The dissipation per unit volume is expressed using a dissipation potential, ψ, which is a function of internal variables associated with rate, damage and plastic process as the following:

$$d = \frac{\partial \psi}{\partial \dot{\varepsilon}_{ij}^v}\dot{\varepsilon}_{ij}^v + \frac{\partial \psi}{\partial \dot{D}_{ij}}\dot{D}_{ij} + \frac{\partial \psi}{\partial \dot{\varepsilon}_{ij}^p}\dot{\varepsilon}_{ij}^p \geq 0 \tag{2}$$

where, $\psi = \psi(\varepsilon_{ij}, \theta, \varepsilon_{ij}^v, \dot{\varepsilon}_{ij}^v, D_{ij}, \dot{D}_{ij}, \varepsilon_{ij}^p, \dot{\varepsilon}_{ij}^p)$

Further, the thermomechanical framework is established for granular system expressing the Helmholtz free energy density and the dissipation potential as the following [21]:

$$W = \frac{1}{V}\sum_{\alpha}^{N} W^{\alpha}(\delta_j^{\alpha}, \delta_j^{v\alpha}, D_j^{\alpha}, \delta_j^{p\alpha}, \theta^{\alpha}) \tag{3}$$

$$\psi = \frac{1}{V}\sum_{\alpha=1}^{N} \psi^{\alpha}(\delta_j^{\alpha}, \delta_j^{v\alpha}, \dot{\delta_j^{v\alpha}}, D_j^{\alpha}, \dot{D_j^{\alpha}}, \delta_j^{p\alpha}, \dot{\delta_j^{p\alpha}}, \theta^{\alpha})$$

where N is the total number of grain-pair interactions, W^{α} and ψ^{α} are the contributions of α-th interaction to the free energy and to the dissipation potential. The grain-scale displacement vector is represented with δ_j^{α}. $\delta_j^{v\alpha}, D_j^{\alpha}$ *and* $\delta_j^{p\alpha}$ are the grain-scale internal variables related to rate dependence, damage and plasticity. Moreover, overall stress, macroscopic Cauchy stress, is derived from Clausius-Duhem inequality as the following:

$$\sigma_{ij} = \frac{\partial W}{\partial \varepsilon_{ij}} = \frac{1}{V}\sum_{\alpha=1}^{N} f_k^{\alpha}\frac{\partial \delta_k^{\alpha}}{\partial \varepsilon_{ij}} \tag{4}$$

where f_k^{α} is the intergranular force that is $f_k^{\alpha} = \frac{\partial W^{\alpha}}{\partial \delta_k^{\alpha}}$.

Furthermore, the micro-scale Clausius-Duhem inequality is derived which considers the α-th interaction as the following:

$$f_j^{\alpha}\dot{\delta}_j^{\alpha} - \dot{W}^{\alpha} - S^{\alpha}\dot{\theta}^{\alpha} = d^{\alpha} \geq 0 \tag{5}$$

The model considers the micro-scale dissipative potential and free energy decomposing into normal and shear components $\psi_n^{\alpha}, \psi_w^{\alpha}$ and W_n^{α}, W_w^{α} respectively, as the following:

$$\psi_n^{\alpha} = \frac{1}{2}\mu_n^{\alpha}\left(\dot{\delta}_n^{v\alpha}\right)^2 + Y_n^{\alpha}\left|\dot{D}_n^{\alpha}\right| + Z_n^{\alpha}\left|\dot{\delta}_n^{v\alpha}\right| \tag{6}$$

$$\psi_w^{\alpha} = \frac{1}{2}\mu_w^{\alpha}\left(\dot{\delta}_w^{v\alpha}\right)^2 + Y_w^{\alpha}\left|\dot{D}_w^{\alpha}\right| + Z_w^{\alpha}\left|\dot{\delta}_w^{v\alpha}\right|$$

where the micro-scale viscosities are represented as μ_n and μ_w. Y and Z are conjugate forces to the grain-scale damage and plastic dissipation. Further, micro-scale free energy is derived as:

$$W_n^{\alpha} = \frac{1}{2}E_1^{\alpha}(\delta_n^{e\alpha})^2 + \frac{1}{2}E_n^{\alpha}(1 - D_n^{\alpha})(\delta_n^{v\alpha})^2(1 - \beta_n^{\alpha}) \tag{7}$$

$$W_w^\alpha = \frac{1}{2} G_1^\alpha (\delta_w^{e\alpha})^2 + \frac{1}{2} G_w^\alpha (1 - D_w^\alpha)(\delta_w^{v\alpha})^2 (1 - \beta_w^\alpha)$$

where the grain-scale stiffnesses are represented as E_1, G_1, E_n, G_w and D_n is the grain-scale damage in the normal direction whereas D_w is the damage in the shear direction. Moreover, constant plastic parameters in shear and normal directions are represented as β_n^α and β_w^α, respectively. Then, the micro-scale constitutive relationships in normal and shear directions are derived as the following (Fig. 3):

$$f_n^\alpha = K_n^\alpha \delta_n^\alpha + \eta_n^\alpha \dot{\delta}_n^\alpha - \zeta_n^\alpha \dot{f}_n^\alpha \tag{8}$$

$$f_w^\alpha = K_w^\alpha \delta_w^\alpha + \eta_w^\alpha \dot{\delta}_w^\alpha - \zeta_w^\alpha \dot{f}_w^\alpha$$

where K is the grain-scale stiffness, η is the grain-scale viscosity parameter and ζ is the grain-scale relaxation parameter which are expressed as the following:

$$\begin{aligned} K_n^\alpha &= \frac{E_1^\alpha E_n^\alpha (1 - D_n^\alpha)}{E_1^\alpha + E_n^\alpha (1 - D_n^\alpha)};\ \eta_n^\alpha = \frac{E_1^\alpha \mu_n^\alpha}{E_1^\alpha + E_n^\alpha (1 - D_n^\alpha)};\ \zeta_n^\alpha = \frac{\mu_n^\alpha}{E_1^\alpha + E_n^\alpha (1 - D_n^\alpha)}; \\ K_w^\alpha &= \frac{G_1^\alpha G_n^\alpha (1 - D_w^\alpha)}{G_1^\alpha + G_w^\alpha (1 - D_w^\alpha)};\ \eta_w^\alpha = \frac{G_1^\alpha \mu_w^\alpha}{G_1^\alpha + G_w^\alpha (1 - D_w^\alpha)};\ \zeta_w^\alpha = \frac{\mu_w^\alpha}{G_1^\alpha + G_w^\alpha (1 - D_w^\alpha)} \end{aligned} \tag{9}$$

The damage in normal and shear directions at grain-scale is expressed as the following:

$$D_n = 1 - e^{-\left|\frac{\left(\delta_n(t) - \frac{f_n(t)}{E_1}\right)}{B_n}\right|};\quad \text{and} \quad D_w = 1 - e^{-\left|\frac{\left(\delta_w(t) - \frac{f_w(t)}{G_1}\right)}{B_w}\right|} \tag{10}$$

where B_n and B_w are damage parameters in normal and shear directions. Besides, the viscosity parameters are expressed considering micro-scale damage as the following:

$$\mu_n(t) = \mu_{n0} e^{-\left|\frac{\left(\delta_n(t) - \frac{f_n(t)}{E_1}\right)}{\beta B_n}\right|}; \quad \text{and} \quad \mu_w(t) = \mu_{w0} e^{-\left|\frac{\left(\delta_w(t) - \frac{f_w(t)}{G_1}\right)}{\beta B_w}\right|} \tag{11}$$

In a later study Misra and Singh [23]. implemented a backward Euler method into the model in order to solve for micro-scale forces. In detail, force-displacement is discretized using backward difference as the following:

$$f_i^t = K_{ij}^{t-\Delta t}\delta_j^t + \eta_{ij}^{t-\Delta t}\delta_j^{t-\Delta t} + \zeta_{ij}^{t-\Delta t} f_j^{t-\Delta t} \tag{12}$$

where the superscript t represents the current time and the superscript $t - \Delta t$ is the previous time step. Finally, the macroscopic constitutive relation at the current time is established based as follows [23, 24]:

$$\sigma_{ij}^t = C_{ijkl}^{t-\Delta t}\varepsilon_{kl}^t + P_{ijkl}^{t-\Delta t}\varepsilon_{kl}^{t-\Delta t} + \tilde{\sigma}_{ij}^{t-\Delta t} \tag{13}$$

In the present study, the user defined nonlinear material model presented above was implemented to the commercial finite element analysis software linking with visual Fortran composer (Intel, Santa Clara, CA).

Finite Element Analysis

Fig. 4 shows the FE model of the disc specimen used in the experiments. To simplify the experimental conditions and reduce computational effort, plane-strain-type condition was implemented in the 3D FE simulation. The plane-strain-type condition was applied by ensuring that element size in the z-direction was the same as the disc thickness, such that the model was single element thick. In addition, the displacement in z-direction was restricted on both the front and back side of the disc. In this manner, both 3D nature of problem is preserved while ensuring

a plane-strain-type loading. We note, however, that the full 3D model will relax the constraints along the thickness direction, thus leading to a somewhat softer behavior, particularly for the case in which the thickness to diameter ratio is large. For the tested specimen, the thickness to diameter ratio is 0.2 and for this case, the 3D effect is expected to be small. Further, to mimic the experimental loading conditions without further augmenting the FE model with interfacial elements to define loading block-disc specimen interaction, a displacement was applied at the rate of 0.0025 mm/increment in y-direction on top and bottom side surfaces in y-direction as an arc of 5° from the disc center as depicted in Fig. 4a. The FE mesh was generated using 4-node linear tetrahedral elements (C3D4). The total number of elements in the FE model were 4483, the number of degrees of freedom were 27333 and the typical CPU time for a simulation 674 sec. The model dimensions were proportional to the dimensions of the experimental specimen.

Results and Discussion

Fig. 5 shows the measured and predicted force-displacement curve for the diametral compression test. The small concave upwards behavior in the measured data is likely due to the hardening effect as the contact area between loading block and the disc specimen increases with loading. It is notable that the damage within the specimen also increases with loading. The softening mechanism due to damage reduces the effect of the hardening mechanism. At higher loading, the softening mechanism dominates leading to failure and fracture of the specimen at an axial force of ~17 N and an axial displacement of ~0.17 mm which is 5% of diameter of the undeformed disc. Since the FE simulation does not account for this initial hardening effect, the predicted curve always shows damage related softening, and a slightly concave downwards behavior in early part of the loading. It is remarkable, however, that the predicted and the observed force-displacement

curves are close suggesting that the model captures the overall behavior quite well. We note that the FE simulation cease once the peak is reached. For post peak response, 2nd gradient models are needed [25, 26]

Fig. 6 shows the snapshots of failure initiation and evolution to fracture in the disc specimen during diametral compression test. From Fig. 6a, we observe the initiation of failure along the diameter collinear with the loading as a discoloration indicated by the arrow marker, which intensifies in Fig. 6b, as the failure process proceeds further. Finally, in Fig. 6c, the fracture develops along the diameter collinear with loading direction rather abruptly, accompanied by another fracture inclined to the direction of loading that grows from circumference inwards and the specimen fails expeditiously. Although, we have shown results for one specimen, it is notable that multiple specimen were tested and similar fracture pattern was observed with some statistical variations. Similar fracture patterns are expected due to the nature of the diametral compression test, in which the maximum tensile action is designed to be orthogonal to the loading direction such that the fracture propagates along the diameter aligned in the loading direction. Such fracture propagation has been further emphasized in our diametral compression test methodology by placing a central hole that provides a weakness location in randomly heterogeneous materials. Furthermore we note that some statistical variations are not unexpected due to natural variability in bones and variability in sample preparation. In the present work, we have focused upon demonstrating that the proposed computational approach is able to well describe the salient features of the fracture phenomena under diametral compression as well as capture the volume dilation behavior observed at the nano-scales of mineralized tissue[5]. The fracture pattern will be further analyzed in the future using digital image correlation (DIC) or other image analysis techniques for obtaining field

measurements, which can then be used for more extensive comparison with the computational results. In this regard, we note that the DIC approach is not always easy to implement and only provides information at the exposed surface. Nevertheless, such an information could be valuable for further model validation.

The development of discoloration zone followed by fracture is an indication that the failure within the specimen was likely preceded the diffuse damage accompanied with the development of dilatation band. These observations are supported by the FE simulation results. In Fig. 7, we show the contour plots of octahedral normal strain and octahedral shear strain which correspond to local volume change and local distortion, respectively. The contour are plotted for the final displacement thresholded by the values at the increment where the specimen reached failure. The grey area in both maps show local volume change and local distortion evolution beyond failure. From Fig. 7a, we can observe that the region along the loading axis starting from edge of the hole underwent dilatation and the same region also experienced high local distortion as seen from Fig. 7b. These maps clearly support the formation of local dilation bands as the precursor to the appearance of micro-sized cracks that propagate into a failure zone (fracture) [5]. However, the simulation also shows that the interpretation of bone fracture [5] need to consider that the 3D nature of loading predicates that dilation is accompanied by shear as seen in Fig. 9. Moreover, for complete fracture modelling, 2nd gradient theories need to be considered [27, 28].

To further illustrate the 3D nature of loading, 6 critical locations, shown in Fig 8, were analyzed in terms of strain path as well as anisotropy evolution. These locations are represented by the elements with assigned numbers in Fig. 8. Element 1 represents the location at upper edge of the hole coinciding the loading axis. As seen from Fig. 9, element 1 follows a strain path in which the octahedral normal strain is always positive indicating volume dilation. It is also remarkable that

the increase of octahedral normal strain far exceeds the octahedral shear strain for this element, indicating that the response is dominated by the dilatational behavior. Element 2 is located close to element 1 but offset somewhat with respect to the loading axis. This element has a similar behavior as element 1 showing that the response of the disc in the proximity of loading axis is dominated by dilatational behavior. Element 3 is also in the vicinity of elements 1 and 2 but it is further offset with respect to the loading axis and is closer to the outer edge of the disc. In contrast to elements 1 and 2, element 3 first under goes contraction followed by dilatation as the localized deformation proceeds from its initiation at the surface of the hole outwards to the loading surface. The dilative behavior in element 3 could presage the development of an alternative strain localization path inclined to the loading direction that is seen experimentally in Fig. 6a. The remainder of the 3 elements were chosen along the axis orthogonal to the loading direction. Element 4, located close to the outer edge, shows an initially contractive response that becomes dilative as the loading progresses, while elements 5 and 6 exhibit predominantly volume contraction.

The varying strain paths at different locations of the disc indicate the evolution of induced anisotropy that manifests as the mineral grain-pairs oriented in various directions within bone experience different amounts of loading. In granular micromechanics, both inherent anisotropy[29] and loading induced anisotropy evolution (caused by micro-damage) are modelled. We note here that in the absence of any data with respect to inherent anisotropy of the specimen, the bone was assumed to be initially isotropic. Fig. 10 shows the contour map of anisotropy index [30] at the applied axial displacement of 0.08 mm, which is approximately 50% of the ultimate failure displacement of ~0.17 mm (see Fig. 5). The anisotropy index is calculated using the method given in [30] upon the basis of the tangent stiffness matrix obtained in the UMAT at the beginning of a

loading increment. The anisotropy index is zero for isotropic materials and takes positive value for anisotropic materials with higher positive value indicating higher degree of anisotropy. In Fig. 10, we have used a logarithmic scale to better visualize the contrast of anisotropy at various location within the disc. While for the majority of the domain, the anisotropy index is close to zero, there are domains where the material becomes anisotropic due to damage although the force-displacement behavior appears to be still within a relatively linear range.

To show the evolution of anisotropy with loading the anisotropy index versus applied axial displacement for at the 6 locations identified in Fig. 8 are shown in Fig. 11. As expected upon the basis of Fig. 10, locations along or in the near vicinity of the loading axis undergo rapidly increasing anisotropy whereas anisotropy change was insignificant at locations along the transverse axis to the loading axis. Anisotropy indices of element 1 through 3 undergo much larger change as seen in Fig. 11 than the elements 4 through 5.

Conclusions and Future Work

The study reported in this paper showed that granular micromechanics based nonlinear material model implemented finite element analysis is capable of capturing load-path dependent local or micro level mechanism observed in the experimental study on disc specimens made of cortical bone. The granular micromechanics model has the advantage of predicting volume change behavior and anisotropy evolution as damage develops within the materials. The numerous elasto-plastic laws proposed in the literature typically do not perform well in predicting these phenomena which are characteristic of granular materials such as bones. Prediction capability of generated

model is convincing looking at results such as local volume change, local distortion and anisotropy evolution comparing to experimental failure patterns of the ring specimen.

We can conclude that the granular micromechanics based nonlinear material model implemented finite element analysis conducted on diametral compression strength test provides more insights about test application and further improvement about the test procedure. When describing mechanical properties of biomaterials it is advantageous to apply physics-based multi-scale models that incorporate the microstructural/ compositional information. Simple but careful models can enable a simultaneous description of behavior at multiple scales and provide insights that are not easily available from measurements.

It is remarkable, though not unexpected, that the material model gives encouraging predictions. We note, however, that these predictions are for a particular loading condition. In the future, this work will be elaborated with an extensive parametric study including effects of rate-dependence, to understand the influence of parameters under more general loading cases.

In this study, the computational work explored the failure in mineralized tissue in depth by providing a practical approach to bridge the scale of observation (millimeter scale) with the building-block scale of apatite crystallites and collagen fibrils, where the granular nature becomes important. The results were assessed by evaluating the models capability of: (1) describing the local (micro-scale) volume compression/dilation behavior, and (2) predicting fracture behavior of millimetric diametral compression experiments. The model describes well the volume change that has been observed experimentally for mineralized tissue at the building block scales. The model also captures the fracture pattern in millimetric diametral compression experiments.

Future analysis will also include 2nd gradient effects, which become increasingly important as the damage develops and a new regime of disordered micro-structures develops [26, 31].

This is particularly significant as the distributed “diffuse” damage develops and, eventually localizes to narrow fracture bands.

Acknowledgements

The authors gratefully acknowledge support for this work from the National Institute of Dental and Craniofacial Research, National Institutes of Health, Bethesda, Maryland, grant number R01DE025476. This research is also supported in part by the United States National Science Foundation grant CMMI -1727433.

References

1. Armstrong S, Geraldeli S, Maia R, et al. Adhesion to tooth structure: a critical review of "micro" bond strength test methods. *Dent Mater* 2010; 26: e50-62. DOI: 10.1016/j.dental.2009.11.155.
2. Marshall SJ, Bayne SC, Baier R, et al. A review of adhesion science. *Dent Mater* 2010; 26: e11-16. DOI: 10.1016/j.dental.2009.11.157.
3. Ye JH, Wu FQ and Sun JZ. Estimation of the tensile elastic modulus using Brazilian disc by applying diametrically opposed concentrated loads. *International Journal of Rock Mechanics and Mining Sciences* 2009; 46: 568-576. DOI: 10.1016/j.ijrmms.2008.08.004.
4. Zaytsev D and Panfilov P. Deformation behavior of human dentin in liquid nitrogen: a diametral compression test. *Mater Sci Eng C Mater Biol Appl* 2014; 42: 48-51. DOI: 10.1016/j.msec.2014.05.011.
5. Poundarik AA, Diab T, Sroga GE, et al. Dilatational band formation in bone. *Proceedings of the National Academy of Sciences* 2012; 109: 19178-19183.
6. Fossen H, Schultz RA, Shipton ZK, et al. Deformation bands in sandstone: a review. *Journal of the Geological Society* 2007; 164: 755-769.
7. Poorsolhjouy P and Misra A. Effect of intermediate principal stress and loading-path on failure of cementitious materials using granular micromechanics. *International Journal of Solids and Structures* 2017; 108: 139-152. DOI: 10.1016/j.ijsolstr.2016.12.005.
8. Kruzic J and Ritchie R. Fatigue of mineralized tissues: cortical bone and dentin. *Journal of the mechanical behavior of biomedical materials* 2008; 1: 3-17.
9. Carrera CA, Chen YC, Li Y, et al. Dentin-composite bond strength measurement using the Brazilian disk test. *J Dent* 2016; 52: 37-44. DOI: 10.1016/j.jdent.2016.07.002.
10. Zaytsev D and Panfilov P. Deformation behavior of human enamel under diametral compression. *Materials Letters* 2014; 136: 130-132.
11. Huang SH, Lin LS, Rudney J, et al. A novel dentin bond strength measurement technique using a composite disk in diametral compression. *Acta Biomater* 2012; 8: 1597-1602. DOI: 10.1016/j.actbio.2011.12.036.
12. Chen YM, Xi TF, Zheng YF, et al. In vitro structural changes of nano-bacterial cellulose immersed in phosphate buffer solution. In: *Journal of Biomimetics, Biomaterials and Tissue Engineering* 2011, pp.55-66. Trans Tech Publ.
13. Carneiro F and Barcellos A. Concrete tensile strength. *Union of testing and research laboratories for materials and structures* 1953; 13.
14. Fairbairn EMR and Ulm FJ. A tribute to Fernando L. L. B. Carneiro (1913-2001) - Engineer and scientist who invented the Brazilian test. *Materials and Structures* 2002; 35: 195-196. DOI: Doi 10.1007/Bf02533589.
15. Li DY and Wong LNY. The Brazilian Disc Test for Rock Mechanics Applications: Review and New Insights. *Rock Mechanics and Rock Engineering* 2013; 46: 269-287. DOI: 10.1007/s00603-012-0257-7.
16. Ramanathan B and Raman V. Split tensile strength of cohesive soils. *Soils and Foundations* 1974; 14: 71-76.
17. Standard Test Method for Splitting Tensile Strength of Intact Rock Core Specimens. ASTM International, 2016.
18. Standard Test Method for Splitting Tensile Strength of Cylindrical Concrete Specimens. ASTM International, 2004.
19. Jonsen P, Haggblad HA and Sommer K. Tensile strength and fracture energy of pressed metal powder by diametral compression test. *Powder Technology* 2007; 176: 148-155. DOI: 10.1016/j.powtec.2007.02.030.
20. Shang C, Sinka IC and Pan J. Modelling of the break force of tablets under diametrical compression. *International Journal of Pharmaceutics* 2013; 445: 99-107.

21. Misra A and Singh V. Thermomechanics-based nonlinear rate-dependent coupled damage-plasticity granular micromechanics model. *Continuum Mechanics and Thermodynamics* 2015; 27: 787-817.
22. Misra A and Poorsolhjouy P. Granular micromechanics model for damage and plasticity of cementitious materials based upon thermomechanics. *Mathematics and Mechanics of Solids* 2015: 1081286515576821.
23. Misra A and Singh V. Nonlinear granular micromechanics model for multi-axial rate-dependent behavior. *International Journal of Solids and Structures* 2014; 51: 2272-2282.
24. Misra A, Singh V and Darabi M. Asphalt pavement rutting simulated using granular micromechanics based rate dependent damage-plasticity model. *International Journal of Pavement Engineering* 2017; (accepted).
25. Placidi L, Barchiesi E and Misra A. A strain gradient variational approach to damage: a comparison with damage gradient models and numerical results. *Mathematics and Mechanics of Complex Systems* 2018; 6: 77-100.
26. Placidi L, Misra A and Barchiesi E. Two-dimensional strain gradient damage modeling: a variational approach. *Zeitschrift für angewandte Mathematik und Physik* 2018; 69: 56.
27. Placidi L and Barchiesi E. Energy approach to brittle fracture in strain-gradient modelling. *Proc R Soc A* 2018; 474: 20170878.
28. Yang Y and Misra A. Micromechanics based second gradient continuum theory for shear band modeling in cohesive granular materials following damage elasticity. *International Journal of Solids and Structures* 2012; 49: 2500-2514. DOI: 10.1016/j.ijsolstr.2012.05.024.
29. Misra A and Poorsolhjouy P. Granular micromechanics model of anisotropic elasticity derived from Gibbs potential. *Acta Mechanica* 2016; 227: 1393-1413.
30. Ranganathan SI and Ostoja-Starzewski M. Universal elastic anisotropy index. *Physical Review Letters* 2008; 101: 055504.
31. Placidi L, Misra A and Barchiesi E. Simulation results for damage with evolving microstructure and growing strain gradient moduli. *Continuum Mechanics and Thermodynamics* 2018: 1-21. DOI: /10.1007/s00161-018-0693-z.
32. Li S, Demirci E and Silberschmidt VV. Variability and anisotropy of mechanical behavior of cortical bone in tension and compression. *Journal of the Mechanical Behavior of Biomedical Materials* 2013; 21: 109-120.
33. Wolfram U, and Schwiedrzik J. Post-yield and failure properties of cortical bone. *BoneKEy Reports* 2016; 5: 829.

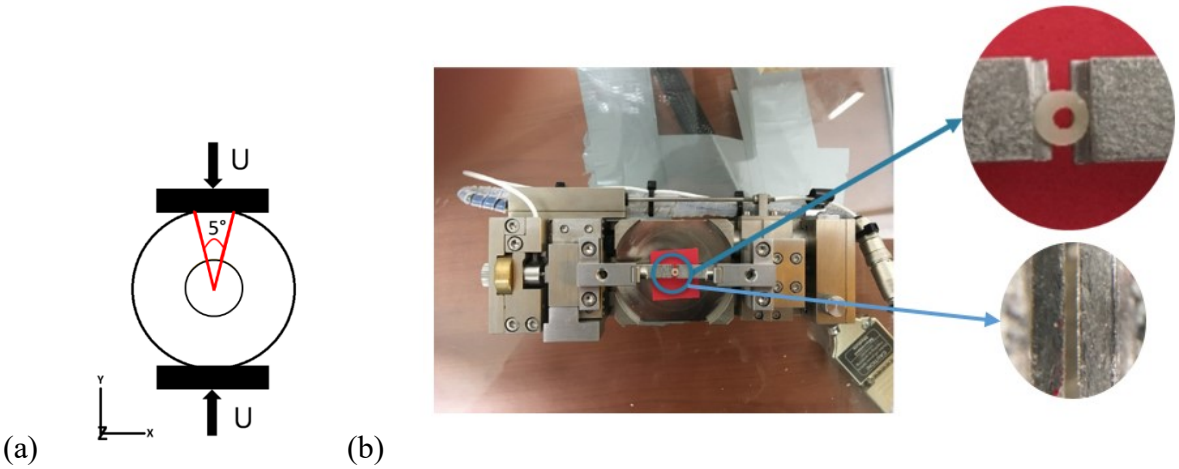

Fig. 1. Test arrangement of diametral compression test. a) Representation of diametral compression test considered in finite element model. b) Physical diametral compression test setup including close-up images showing the placement of the specimen and the parallel alignment of the load platens.

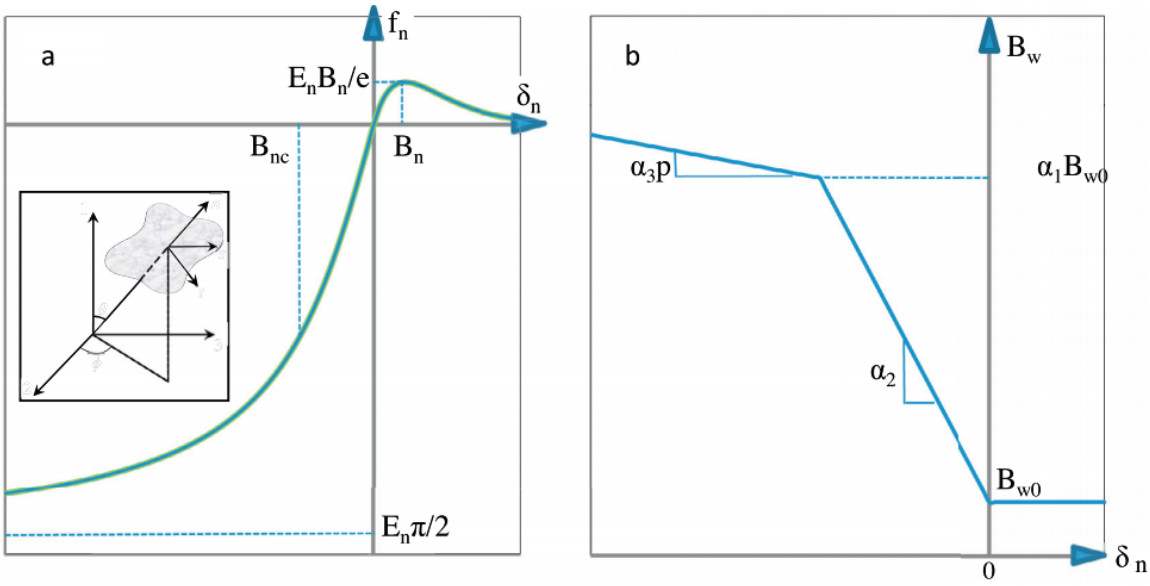

Fig. 2. a) Intergranular normal force with respect to intergranular normal displacement where the inset presents the local coordinates. b) Shear damage parameter with respect to intergranular normal displacement [7]

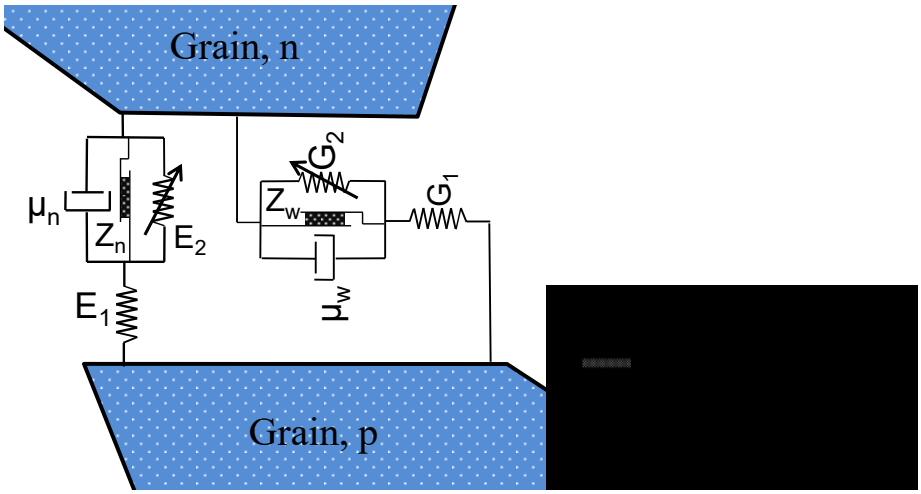

Fig. 3. Representation of the rheological model at micro-scale.

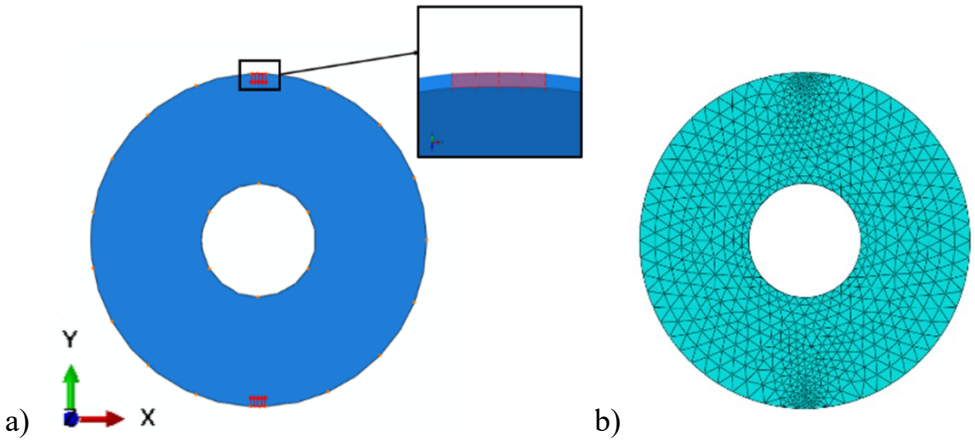

Fig. 4. Finite element model of the ring specimen. a) Displacement loading applied in the model. b) Meshed geometry of the ring model.

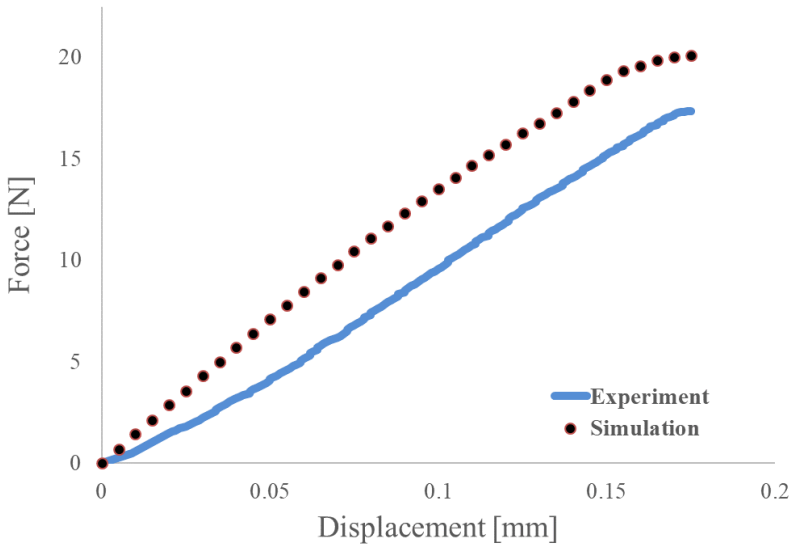

Fig. 5. Force-displacement curve of the ring specimen subject to diametral compression test.

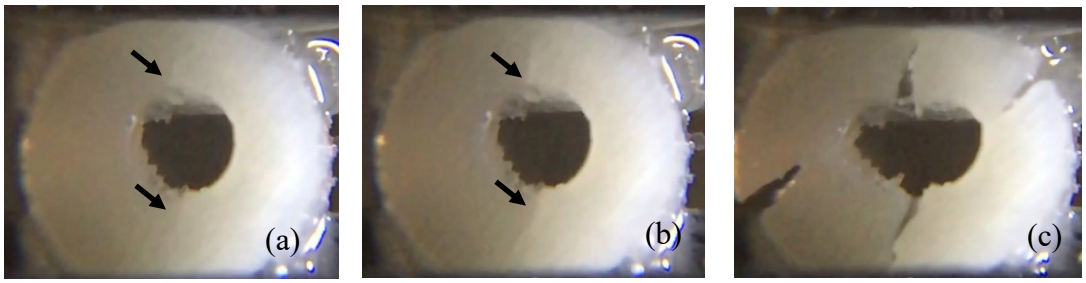

Fig. 6. Initiation and evolution of failure within the ring specimen during diametral compression test. a) Undeformed specimen. b) Initiation of microcracks. c) Fractured specimen.

(a) (b)

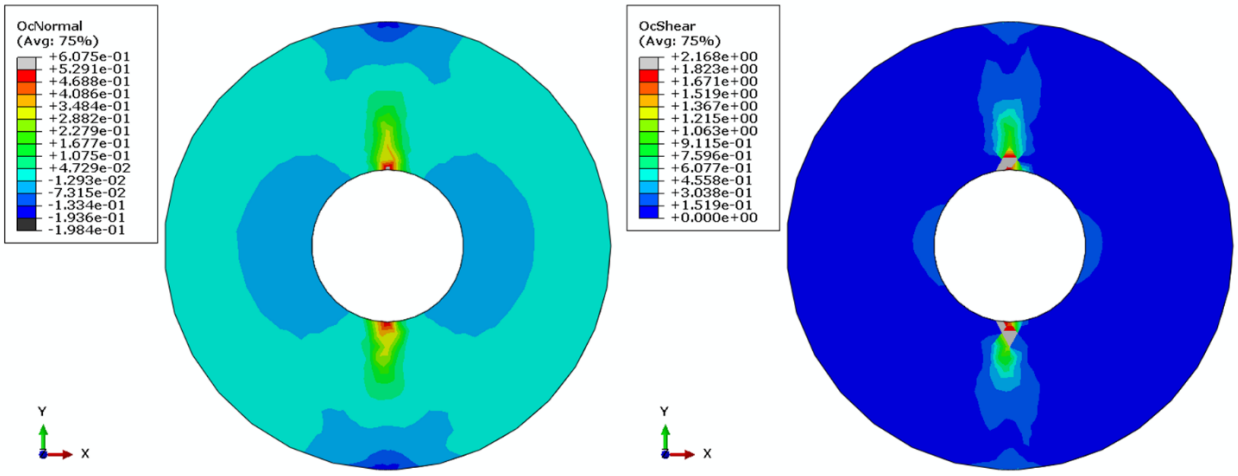

Fig. 7. Evolution of local volume change and local distortion within the specimen represented with octahedral normal and octahedral shear strain maps, respectively, based up FE analysis.

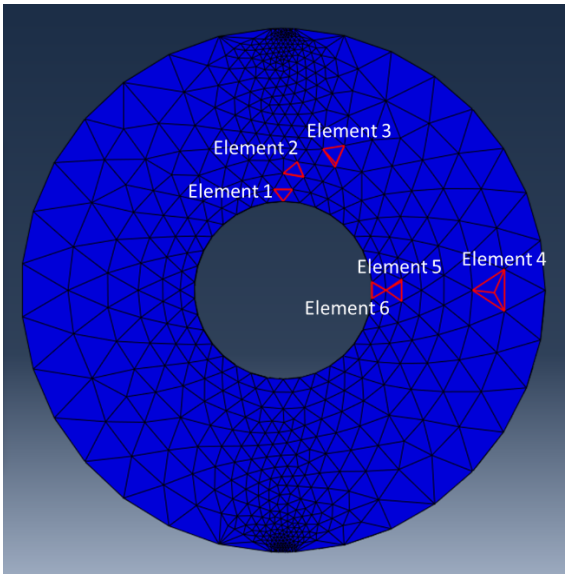

Fig. 8. Element labels on various critical locations selected in finite element analysis on the ring model with bone-like material properties.

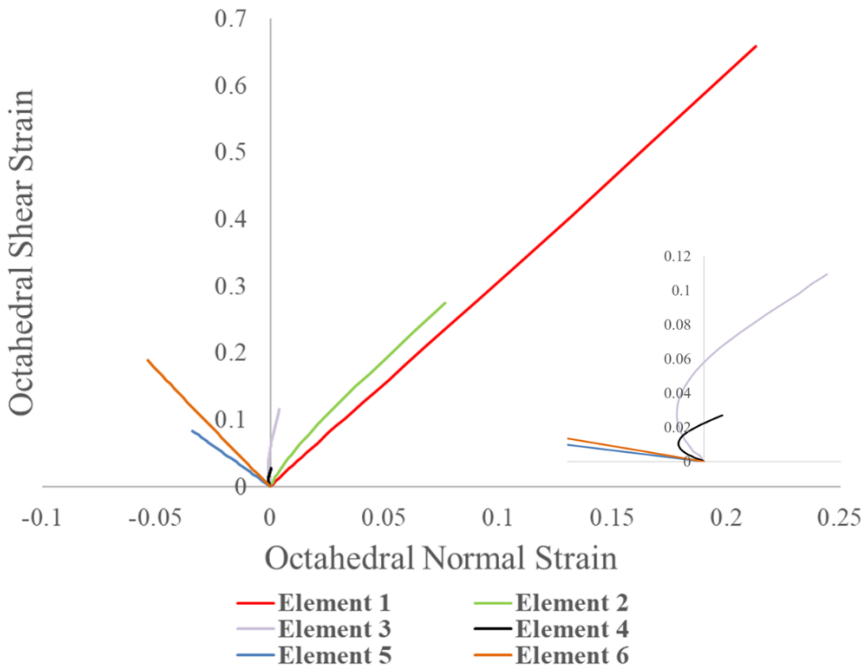

Fig. 9. Strain paths of the selected critical locations in terms of octahedral shear strain with respect to octahedral normal strain based on finite element analysis on the ring model with bone-like material properties.

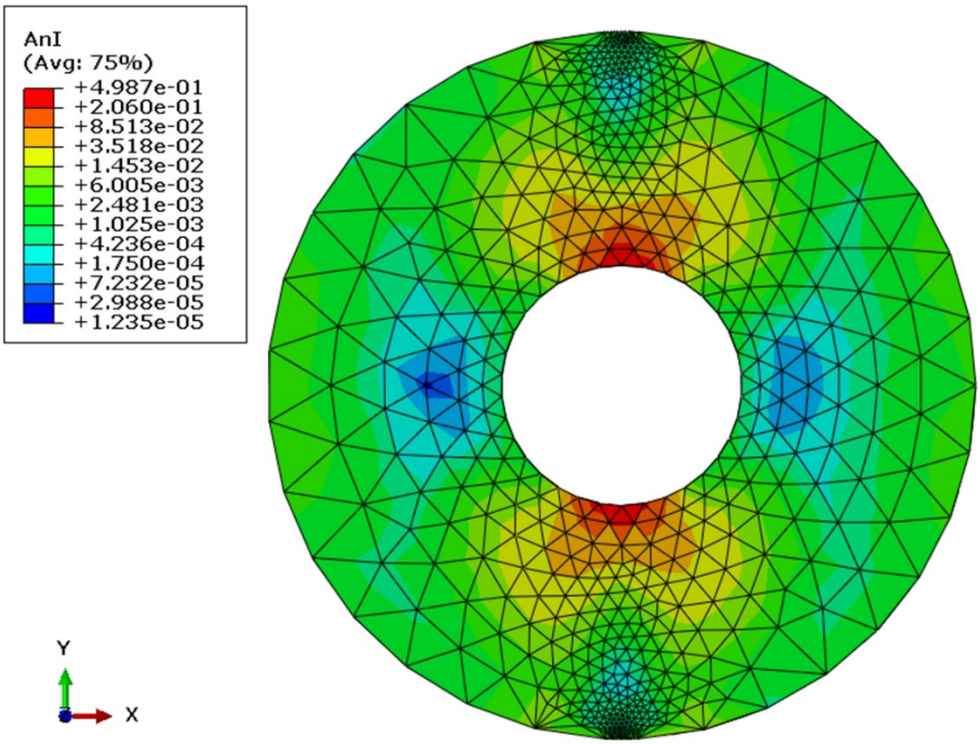

Fig. 10. Evolution of anisotropy within the specimen represented with anisotropy index map based on finite element analysis on the ring model with bone-like material properties.

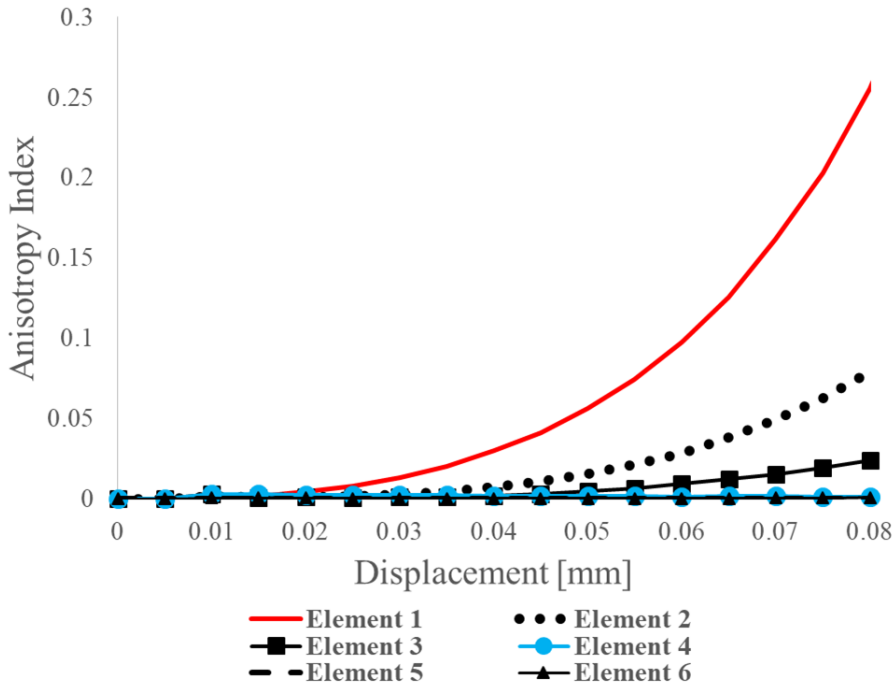

Fig. 11. Anisotropy evolution at the selected critical locations in terms of anisotropy index with respect to displacement based on finite element analysis on the ring model with bone-like material properties.